Journal of
Materials Chemistry B

Materials for biology and medicine

Accepted Manuscript

This article can be cited before page numbers have been issued, to do this please use: Y. Lu, X. Zhang, X. Mao and Y. Huang, *J. Mater. Chem. B*, 2019, DOI: 10.1039/C9TB00797K.

ROYAL SOCIETY OF CHEMISTRY

rsc.li/materials-b

View Article Online
DOI: 10.1039/C9TB00797K

ARTICLE

Engineered FeCo alloy@N-doped carbon layers through directly pyrolyzing Prussian blue analogue - New peroxidase mimetic for chemiluminescence glucose biosensing

Received 00th January 20xx,

Accepted 00th January 20xx

DOI: 10.1039/x0xx00000x

Yuwan Lu,[a] Xiaodan Zhang,[a] Xuanxiang Mao,[a] Yuming Huang*[a]

We reported the synthesis of FeCo alloy@N-doped carbon layers (FeCo@NC), a new peroxidase mimetic, by directly pyrolyzing Fe^{III}-Co Prussian blue analogue (Fe^{III}-Co PBA). The FeCo@NC composite shows excellent peroxidase-like activity due to highly active FeCo alloy, M-N species (Co-N and Fe-N) and N-doped carbon layers with hierarchical pore nanostructures that were formed via a simple heat treatment of Fe^{III}-Co PBA without additional C and N sources. In particular, the obtained FeCo@NC hybrids presented high CL activity with more than 85-fold enhancement on the CL emission of H_2O_2–luminol system, and long-term stability as compared with FeCo alloys nanoparticles. The CL response showed a linear range of 0.01–40 μM H_2O_2 with a limit of detection of 2.5 nM. When coupled with glucose oxidase, we developed a new CL sensing method for the detection of glucose in the linear range of 10 nM to 10 μM with the detection limit of 8.5 nM. This FeCo@NC-based glucose biosensor displays a fastness, high precision and good reproducibility when utilized to real biological samples. Expectedly, the FeCo@NC as new peroxidase mimetic promises great potential for monitoring glucose level in clinical diagnosis.

1. Introduction

Diabetes is known as a group of metabolic diseases related to a glucose metabolic disorder arising from insulin deficiency or resistance,[1] and has become the second killer of modern diseases. According to International Diabetics Foundation, 1.3 million people died of diabetes and complications in China in 2015, which was the largest in the world. The direct manifestation of diabetes is chronic hyperglycemia, which can lead to a variety of complications, including heart disease, kidney failure, nerve damage, limb amputation and so on.[2,3] As diabetes is closely related to the blood glucose concentration, therefore, the rapid, sensitive and accurately determination of the blood glucose concentration is critically important for monitoring and managing diabetes.

In the past decades, various glucose sensing techniques have been developed, such as spectrophotometry, fluorometry, electrochemistry, and chemiluminescence (CL).[4-8] Among them, CL is considered to be one of the most effective and convenient methods for glucose detection due to its outstanding features, such as simple instrument with no excitation light source, high sensitivity, low detection limit, rapid analysis, and easy operation.[9,10] Although CL has been widely investigated in chemical and biological applications, the typical CL systems usually suffer from low efficiency in converting chemical energy into light, greatly limiting its further development in analytical applications.[11] In the last few decades, enormous efforts have been dedicated to exploit novel CL systems and fabricate functional materials with unique catalytic properties to enhance the CL efficiency. Fortunately, with the development of CL biosensors, a well-known luminol–H_2O_2 CL platform, catalyzed by peroxidase, can be conveniently adopted since many peroxidase mimics have been developed. It has been demonstrated that metal or alloy nanoparticles could greatly enhance CL emission of luminol–H_2O_2 system. For instance, Liu's group synthesized the peroxidase-like gold nanoparticle and Yu's group synthesized PtCox/graphene nanocompsites with a strong catalytic effect on luminol–H_2O_2 CL system.[12,13] Dendritic Au-Ag bimetallic nanoparticles with CL activity were synthesized by He's group.[14] However, the drawback of easy oxidation in the air hinders the wide applications of metal NPs. In contrast, alloy materials were proved to have superior catalytic properties as compared with the pure metal NPs for synergistic catalysis over alloy NPs.[15]

Since the carbon-encapsulated materials were firstly synthesized in 1993,[16] they have attracted remarkable interests in many fields because of their interesting properties and potential applications. It is generally considered that carbon-coated composites are more stable by the protection of carbon layer. In addition, previous studies indicated that nitrogen doping was an effective way to tailor electron-donor properties and modulate the surface chemistry of the sp^2 carbon structure due to the larger electronegativity of nitrogen (3.04) in comparison to carbon (2.55), which are favorable for its catalytic properties.[17] Thus, if we fabricate the nitrogen-doped

[a] The Key Laboratory of Luminescence and Real-Time Analytical Chemistry, Ministry of Education, College of Chemistry and Chemical Engineering, Southwest University, Chongqing 400715, China.
Corresponding author. E-mail: ymhuang@swu.edu.cn

† Electronic Supplementary Information (ESI) available. See DOI: 10.1039/x0xx00000x

View Article Online
DOI: 10.1039/C9TB00797K

carbon composites-encapsulated alloy NPs, it would be expected to be a highly active and stable catalyst with high CL activity.

Inspired by the above idea, here, we report a simple, facile, and green strategy to prepare graphitic layers encapsulated FeCo alloys NPs hybrid (denoted FeCo@NC) by direct carbonization of Fe^{III}-Co Prussian blue analogue. The Fe^{III}-Co Prussian blue analogue was selected due to the following reasons. (1) Its organic ligand –CN provides both carbon and nitrogen sources for forming nitrogen-doped carbon, hence, no additional C and N sources are needed. (2) Simple thermal treatment of Fe^{III}-Co PBA in N_2 atmosphere produces bimetal FeCo alloy NPs. Meanwhile, according to the previous report, Fe-N/C and Co-N/C were recognized to efficient catalytic activity sites.[18] The as-prepared FeCo@NC hybrids were characterized by transmission electron microscopy (TEM), X-ray diffraction (XRD), Raman spectrum, and X-ray photoelectron spectra (XPS). The obtained FeCo@NC hybrids exhibited outstanding peroxidase mimetic activity due to N-doping and the unique structure, and presented high CL activity with more than 85-fold enhancement on the CL emission of H_2O_2–luminol system. As a proof-of-concept application, by coupling with glucose oxidase, we have developed a new flow-injection CL sensing method for the sensitive and rapid detection of glucose. The results indicated that the FeCo@NC hybrids-based nanozyme exhibited an outstanding performance for CL glucose sensing, including wide linear range of 10 nM – 10 μM, low detection limit of 8.5 nM, fast response, and long-term storage stability. Impressively, the proposed method was successfully used to the detection of glucose in human serum samples with high precision and good reproducibility.

2. Experimental section

2.1. Material and reagents

All reagents and solvents were obtained commercially and used without further purification. Potassium hexacyanocobaltate (III) (99%), H_2O_2 (30%), $FeCl_3$•$6H_2O$, $CoCl_2$·$6H_2O$, $K_4[Fe(CN)_6]$·$3H_2O$, sodium azide, thiourea, ascorbic acid (AA) were obtained from Chongqing Taixin Chemical Co., Ltd. (Chongqing, China). Glucose oxidase (GOx, *EC*1.1.3.4.47, 200 U/mg) was purchased from Sigma-Aldrich (Shanghai, China) and stored at 4 °C. Superoxide dismutase (SOD, 20000 U/mg) was purchased from Macklin Biochemical Co., Ltd. (Shanghai, China). Glucose, fructose, lactose, sucrose, maltose and starch were purchased from Sinopharm Chemical Reagent Co., Ltd. (Shanghai, China). Luminol was obtained from Merck (Germany). Human serum samples were from the Ninth People's Hospital of Chongqing (Beibei, Chongqing). Ultra-filtration tubes with cutoff molecular weight of 30 kDa were purchased from Millipore Corporation (Billerica, MA 01821, USA). Ultra-pure water was prepared in our lab.

2.2. Apparatus

The CL spectra were recorded with an F-2700 fluorescence spectrophotometer (Hitachi, Japan) under the model of fluorescence scan by turning off the excitation light source. The scanning electron microscope (SEM) images were taken on Hitachi model S-4800 field emission scanning electron microscope (Hitachi, Japan) with an accelerating voltage of 20 kV. The XRD pattern was recorded on an XD-3 X-ray diffractometer (PuXi, Beijing, China) with the conditions of nick-filtered CuK α radiation (λ = 0.15406 nm) at a scanning rate of 4°/min from 5° to 100° (2θ). Fourier transform infrared (FT-IR) spectra were obtained by a Tenson 27 Fourier Transform Infrared spectrometer (Bruker, Germany). Thermogravimetric (TG) analysis were conducted on a TA-SDT Q600 (Texas Instruments, Inc., New Castle, DE) in the temperature range of 30–800 °C at a heating rate of 10 °C/min. The TEM images were obtained with a Tecnai G2 F20 electron microscope (FEI, USA). XPS characterizations were recorded by a VG Multilab 2000X instrument (Thermal Electron, USA). Raman spectra were obtained on a Renishaw Raman microscope (Renishaw inVia Raman microscope, UK). The specific surface area was determined by the Brunauer-Emmett-Teller (BET) method based on the N_2 adsorption-desorption isotherm data, which were obtained with an ASAP 2020 Micromeritics instrument (Maike, USA) at 77 K. The CL detection was carried out on a computer controlled IFFS-A/MCDR-A flow injection CL analyzer (Xi'an, China). Electron spin resonance measurement was

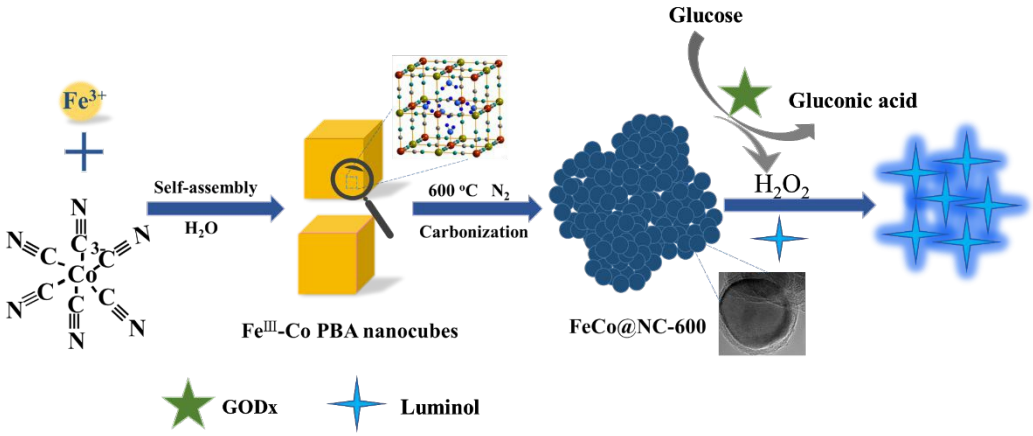

Scheme 1. Schematic of the preparation process of FeCo@NC-600 and its use as peroxidase mimetic for glucose sensing by CL.

carried out using a Bruker ESR spectrometer (A300-10/12, Germany). Amperometric response was measured on a CHI660E electrochemical workstation (Shanghai Chenhua Device Company, China). The schematic of the CL detection system utilized in the present work was provided in Fig. S1 (ESI†).

2.3. Synthesis of Fe^{III}-Co PBA and FeCo alloy@nitrogen-doped carbon composites

$Fe[Co(CN)_6]$ (Fe^{III}-Co PBA) was prepared based on previous works,[19,20] with slight modification. In brief, $FeCl_3 \cdot 6H_2O$ (0.6758 g) and $K_3[Co(CN)_6]$ (0.8308 g) were dissolved in 50 mL of deionized (DI) water to form a clear solution. Subsequently, the mixed solution was stirred for 30 min and aged for 24 h at room temperature. Finally, the pale yellow Fe^{III}-Co PBAs solid were obtained by centrifugation, then washed with deionized water for least three times and dried at 333 K.

To prepare FeCo alloy@nitrogen-doped carbon composites (FeCo@NC-X, X represents the carbonization temperature), 100 mg of Fe^{III}-Co PBA was pyrolyzed in a horizontal tubular furnace in N_2 atmosphere at different temperature in the 400 °C to 900 °C range for 2 h with heating rate of 2 °C/min. The resultant products were denoted FeCo@NC-400, FeCo@NC-500, FeCo@NC-600, FeCo@NC-700, FeCo@NC-800, and FeCo@NC-900, respectively.

2.4. Synthesis of Co@NC and Fe@NC

For comparison, we synthesized Fe@NC and Co@NC. In brief, $FeCl_3 \cdot 6H_2O$ (0.6758 g) and $K_4[Fe(CN)_6] \cdot 3H_2O$ (1.056 g) were dissolved in 50 mL of deionized water to form a clear solution, and then the mixed solution was stirred for 30 min and aged for 24 h at room temperature. After reaction, the mixture was centrifuged, and the PB solid was collected by centrifugation. Similarly, $CoCl_2 \cdot 6H_2O$ (0.5948 g) and $K_3[Co(CN)_6]$ (0.8308 g) were dissolved in 50 mL of deionized water to form a clear solution, and then stirred for 30 min and aged for 24 h at room temperature. Finally, the pale pink Co^{II}-Co PBA solid was obtained by centrifugation. After calcining the PB and the Co^{II}-Co PBA at 600 °C in N_2 for 2 h, the Fe@NC and Co@NC were obtained.

2.5. General procedure for glucose detection

The detailed procedure for CL detection was provided in Electronic Supplementary Information. Glucose detection was performed as follows: 0.1 mL of 1 mg/mL GOx and 0.1 mL of glucose with different concentrations in 0.5 mL of PBS buffer (pH 7.0) were incubated at 37 °C for 30 min. And then, the resulting mixture was diluted to 10 mL by water, and used for standard curve measurement. For glucose determination in serum, the samples were first treated by ultra filtration with 5 kDa Amicon cell at 3000 rpm for 10 min. The filtrate was diluted properly with PBS buffer (pH 7.0). Then 0.1 mL of the diluted filtrate was added into 0.1 mL of 1 mg/mL GOx. The obtained mixture was incubated at 37 °C for 30 min and then used for the glucose measurement.

2. Results and discussion

3.1. Preparation and characterization of Fe^{III}-Co PBA and FeCo@NC

The procedures for fabricating FeCo@NC are illustrated in Scheme 1. Crystalline Fe^{III}-Co PBA with a well-defined nanocubic structure was prepared firstly. SEM image in Fig. S2A (ESI†) shows that the obtained Fe^{III}-Co PBA nanocubes have a uniform distribution with an average size of ~ 300 nm. The XRD pattern in Fig. 2A reveals that all characteristic diffraction peaks of the as-synthesized sample at 14.4° (111), 17.4° (200), 24.7° (220), 35.2° (400), 39.5° (331), and 43.5° (422) are well matched with typical Fe^{III}-Co PBA (JCPDS No. 89-3736),[21] confirming the successful synthesis of Fe^{III}-Co PBA by co-precipitation method. After carbonization at 600 °C for 2 h, the as-obtained FeCo@NC-600 exhibits quite different morphology (Fig. S2B, ESI†) and XRD patterns (Fig. 2A) due to its intrinsic chemical composition. Fe and Co atoms from the precursor form FeCo alloy nanoparticles, while CN group linkers served as both carbon and nitrogen sources form nitrogen doped carbon composites. The XRD peaks are located at 44.9°, 65.3°, and 82.6° (Fig. 2A), corresponding to (110), (200) and (211) planes of FeCo alloy (JCPDS No. 49-1567), respectively.[22] TEM image (Fig. 1A) illustrates that the composite is composed of graphitic carbon layers encapsulated small alloy particles. Meanwhile, the lattice fringes can be clearly seen in the HRTEM image (Fig. 1B), in which the 2.06 Å can be assigned to the (110) plane of CoFe nanoalloy,[23] and the 3.43 Å belongs to (002) plane of graphite.[24]

Fig. S3 shows the FT-IR spectra of Fe^{III}-Co PBA and FeCo@NC-600. The absorption band at 2166 cm^{-1} is attributed to the characteristic C≡N stretching vibration of Fe^{III}-Co PBA.[25] The absorption bands of H-O-H bending mode at 1610 cm^{-1} and O-H stretching mode at 3390 cm^{-1} demonstrate the presence of water molecules in the structure of Fe^{III}-Co PBA[26] and absorption bands at 499 cm^{-1} are due to the formation of Co-CN-Fe.[27] After pyrolysis, it is obvious that the absorption peaks of C≡N and Co-CN-Fe disappear. This indicates the frame structure of Fe^{III}-Co PBA has been completely destroyed under condition of high temperature calcinations, leading to successful formation of FeCo@NC.

To gain a better understanding of the surface element compositions and the valence states of the FeCo@NC-600 catalysts, XPS analysis was carried out. The full XPS spectrum (Fig. S4, ESI†) highlights the existence of Fe, Co, N, and C

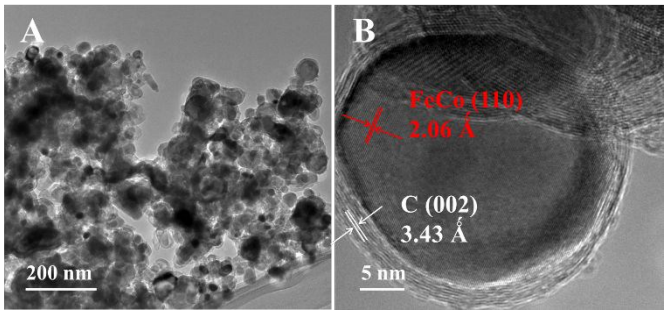

Fig. 1. (A) TEM image and (B) HRTEM image of the FeCo@NC-600.

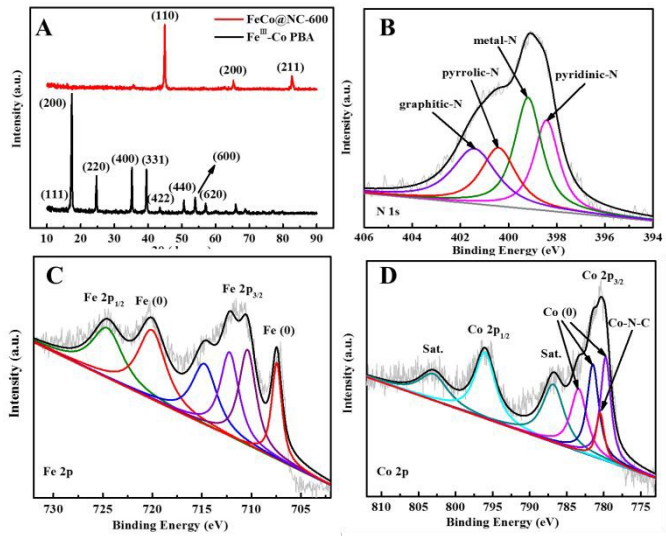

Fig. 2. (A) XRD patterns of the synthesized Fe^{III}-Co PBA (black) and FeCo@NC-600 (red). (B) N 1s, (C) Fe 2p and (D) Co 2p XPS of FeCo@NC-600 sample.

element. The high resolution XPS spectra for N 1s, Fe 2p, Co 2p were plotted. As shown in Fig. 2B, N 1s spectrum is deconvoluted into four characteristic peaks, corresponding to pyridinic-N (398.42 eV), metal-N (399.19 eV), pyrrolic-N (400.41 eV) and graphitic-N (401.42 eV),[28,29] respectively. This suggests possible formation of N–doped graphite carbon layers. From the high-resolution XPS spectra of Fe 2p shown in Fig. 2C, two peaks at 707.3 eV and 719.5 eV are ascribed to the metallic state of Fe,[30] respectively. In addition, the peaks at 711.6 eV and 725.5 eV are the characteristic oxide Fe $2p_{3/2}$ and $2p_{1/2}$, respectively.[31] In Fig. 2D, Co $2p_{3/2}$ can be fitted into four peaks. The binding energies at 778.9, 780.5 and 783.4 eV correspond to metallic Co,[32,33] while the binding energy at 781.5 eV is attributed to Co-N-C.[34] In addition, energy-dispersive spectroscopy (EDS) (Fig. S5, ESI†) shows that the atomic ratio of Fe (at% 29.15) to Co (at% 25.84) in synthesized FeCo@NC was close to 1:1 (Table S1, ESI†), which is very consistent with the theoretical ratio of Fe to Co in $Fe[Co(CN)_6]$. It is noted that the surface C content based on XPS is 71.87%, while it is 36.41% in terms of EDS. Similarly, the surface N content measured by XPS (7.89%) is higher than that by EDS (2.61%). This is probably because nitrogen atoms are mainly doped in the surface carbon layer. However, the surface contents of Fe and Co estimated by XPS are much lower than those from DES. This is probably because FeCo alloy NPs are mainly wrapped in the nitrogen-doped carbon layer.[35] The result is also consistent with the observation from HRTEM that the FeCo nanoparticles are surrounded by graphitic layer. On the basis of above results, we conclude that FeCo@NC have been successfully synthesized through this facile strategy.

Fig. S6 (ESI†) shows the Raman spectra of the FeCo@NC obtained at different carbonization temperature in the 400 °C to 900 °C range. Two peaks centered at 1351 and 1582 cm^{-1} match well with the D and G bands for carbon.[36] When the carbonization temperature increases, the I_D/I_G value decreases gradually, indicating the increase of graphite carbon content. Thermogravimetric result (Fig. S7, ESI†) showed that the decomposition and carbonization of Fe^{III}-Co PBA mainly took place at the temperature in the 500 °C – 600 °C range. The sharp weight loss at 575 °C was attributed to the decomposition of C≡N bond.[37]

The porous structures of the Fe^{III}-Co PBA precursor and FeCo@NC-600 were investigated by the N_2 adsorption-desorption isotherms at 77 K (Fig. S8, ESI†). Both the synthesized Fe^{III}-Co PBA and FeCo@NC-600 exhibit type-IV isotherm. The characteristic hysteresis loop suggests the existence of mesoporous structure in Fe^{III}-Co PBA and FeCo@NC-600. The Brunauer-Emmett-Teller (BET) surface area of Fe^{III}-Co PBA and FeCo@NC-600 are 42.84 m^2/g and 37.63 m^2/g (Table S2, ESI†), respectively. It is noted that the specific surface area of Fe^{III}-Co PBA does not change obviously after calcining in N_2. From the pore size distribution curves, there are two peaks at about 3.5 nm and 50.0 nm (inset in Fig. S8, ESI†). Interestingly, the peak at about 3.5 nm becomes more prominent, suggesting generation of more mesopores after pyrolysis, leading to total pore volume increase from 0.12 cm^3/g to 0.16 cm^3/g (Table S2, ESI†). These results prove the existence of mesopores and macropores in the FeCo@NC-600 with hierarchical pore structure, which is in favour of mass transport and exposing more catalytic active sites.

3.2. The peroxidase-like activity of FeCo@NC

The mimic enzyme activity of FeCo@NC was first examined by performing typical reactions using typical substrates, such as TMB, OPD, and ABTS. As shown in Figs. 3A, B, and C, direct oxidation of these substrates by dissolved oxygen in the absence of FeCo@NC-600 or H_2O_2 produces negligible absorbance, suggesting the very weak oxidase-like activity of FeCo@NC-600. However, an intensive color reaction occurs

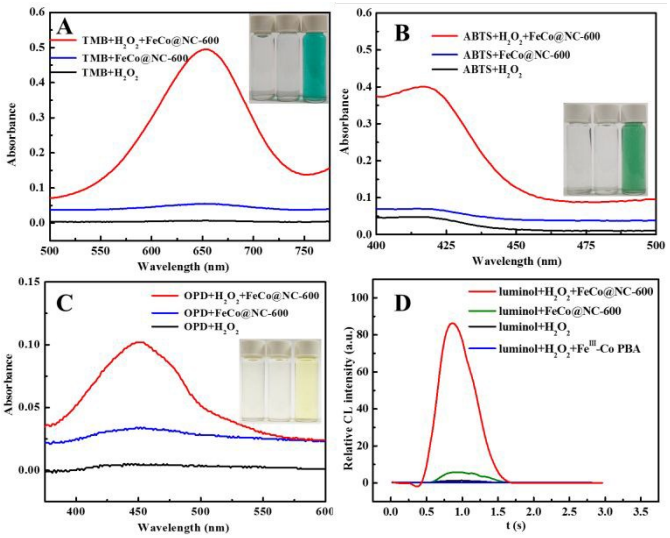

Fig. 3. (A) UV-vis adsorption spectra of TMB in the presence and absence of H_2O_2 and FeCo@NC-600; (B) UV-vis adsorption spectra of ABTS in the presence and absence of H_2O_2 and FeCo@NC-600; (C) UV-vis adsorption spectra of OPD in the presence and absence of H_2O_2 and FeCo@NC-600. Inset: Photographs of corresponding solutions. Reaction conditions: 0.1 mM TMB (ABTS, OPD); 10 mg/L FeCo@NC-600; pH 3.5; 20 min reaction at room temperature; (D) CL kinetic characteristic of luminol in different systems. Reaction conditions: 10 μM luminol in 0.1 M Na_2CO_3-$NaHCO_3$ buffer (pH 11.3); 0.5 μM H_2O_2; 10 mg L^{-1} FeCo@NC-600.

View Article Online
DOI: 10.1039/C9TB00797K

when FeCo@NC-600, substrate and H_2O_2 coexist (insets in Figs. 3A, B, and C). Furthermore, the UV-Vis spectra show the characteristic absorbance peaks of three substrates. The results indicate that FeCo@NC has peroxidase-like catalytic activity. Furthermore, as compared with the monometallic Fe@NC and Co@NC, the FeCo@NC hybrid shows remarkably enhanced peroxidase-like activity (Fig. S9, ESI†), indicting the synergistic effect between Co and Fe[4,24] in the FeCo@NC-600.

Based on the various characterization results, the excellent peroxidase-mimicking activity of FeCo@NC is probably attributed to the following reasons. (1) The active sites, such as Fe-N and Co-N species, were present in the FeCo@NC, which were considered to be the highly efficient enzyme-like catalytic sites (such as peroxidase mimetics,[38,39] SOD mimetics[40] etc). (2) Introducing N atom into carbon structure induces charge delocalization and increases electron cloud density, leading to enhancing catalytic activity.[41-42] Moreover, the encapsulated FeCo alloy NPs can donate electrons to the N-doped carbon layers and further create abundant active sites.[43] (3) The presence of N-doped carbon encapsulating layer on FeCo not only prevents the alloy NPs from oxidation when exposed to air, but also remarkably improves the stability of catalysts and avoided particle aggregation. Thus, the active sites were further dispersed to enhance the catalytic activity. (4) The high I_D/I_G band intensity ratio of the samples implies large amounts of defects in FeCo@NC. This is beneficial to electron transfer through the catalyst during reduction of H_2O_2.[44,45] (5) The hierarchical pore structure of FeCo@NC is benefit not only for rapid diffusion[46,47] of H_2O_2 to the catalytic active sites, but also exposing the catalytic active sites as far as possible and enhancing catalytic activity.

In order to understand the origin of FeCo@NC nanozyme, amperometric responses of the Fe@NC, Co@NC FeCo@NC modified glassy carbon electrodes toward reduction of H_2O_2 were studied. As shown in the Fig. S10A (ESI†), the FeCo@NC, Fe@NC and Co@NC exhibit an electrocatalytic activity in reduction of H_2O_2 and the ability to transfer electrons follows the order of FeCo@NC > Co@NC > Fe@NC. Meanwhile, the experimental results of reactive oxygen species scavenging and the ESR spectra (Figs. S10B, C, and D, ESI†) in the FeCo@NC-H_2O_2 system indicate the co-existence of •OH radicals and $•O_2^-$ radicals during reaction. Based on the above results, a possible mechanism of the peroxidase activity of FeCo@NC is ascribed to its activation of H_2O_2 to produce reactive oxygen species, including •OH and $•O_2^-$. The strong oxidizing ability of $•O_2^-$ and •OH can catalytic oxidize TMB to oxidized TMB.

To further prove peroxidase-mimicking activity, the catalytic effect of FeCo@NC-600 on the luminol–H_2O_2 CL system was investigated. As shown in Fig. 3D, no obvious CL emission is recorded by mixing luminol with H_2O_2 in alkaline media in the absence or presence of Fe^{III}-Co PBA. Similarly, a very weak CL signal is produced from the reaction of luminol with FeCo@NC-600. However, when introducing FeCo@NC-600 into the mixing solution of luminol with H_2O_2, an intense CL signal (about 85-fold enhancement) is produced, suggesting that FeCo@NC-600 exhibits strong catalytic effect on the luminol–H_2O_2 reaction. Besides, the CL reaction is very fast because the CL intensity rapidly reaches the maximum value, within 1 s after injecting the FeCo@NC-600.

To get a deep insight about the effect of pyrolysis temperature on the performance of FeCo@NC, the catalytic CL activity of FeCo@NC obtained at different temperature in the 400-900 °C was explored. The temperature dependence of CL activity of FeCo@NC is plotted in Fig. S11 (ESI†). It is clear the FeCo@NC-600 shows the highest catalytic CL activity. This is because when the pyrolysis temperature is 400 °C or 500 °C, the N-doped graphene carbon layers is not well formed (Fig. S6, ESI†) due to inadequate decomposition of C≡N group in PBA (Fig. S7, ESI†), demonstrating that graphene plays a significant role in enhancing the catalytic performance of FeCo@NC.[48] However, when the pyrolysis temperature is above 600°C, the CL activity of FeCo@NC is declined, which is related to the decline of the doping-N content.[43] The N contents of FeCo@NC-600, FeCo@NC-700, FeCo@NC-800, and FeCo@NC-900 by XPS are 7.98%, 6.66%, 2.82% and 1.93% (Table S3). This is consistent with activity trend of the above catalysts. In addition, the high N-doping content can lead to a large density of defects with highest I_D/I_G value in FeCo@NC-600. These defects serve as active sites and accelerate the catalytic reaction.[24,43] Above result also confirms the synergistic effect between FeCo alloy and N-doped graphene carbon and its key role in controlling the catalytic activity of the above catalysts. Therefore, 600 °C was selected as the optimal pyrolysis temperature for synthesis of FeCo@NC.

To gain more insight into the CL mechanism, CL spectrum and CL quenching experiments were studied. In the luminal–H_2O_2–FeCo@NC-600 system, the maximum emission wavelength was around 425 nm (Fig. 4A). This suggests that the CL emitter was still the excited-state 3-aminophthalate anion (3-APA*) and the FeCo@NC-600 only functions as a catalyst. The experimental results of reactive oxygen species scavenging prove that introducing ascorbic acid, thiourea or superoxide dismutase into the luminol–H_2O_2–FeCo@NC-600 system caused significant decline in CL signal, while sodium azide did minor variance in CL response (Fig. 4B). The result demonstrates that both •OH and $•O_2^-$ play major role in CL reaction. Furthermore, the result of nitrogen-saturated and oxygen-

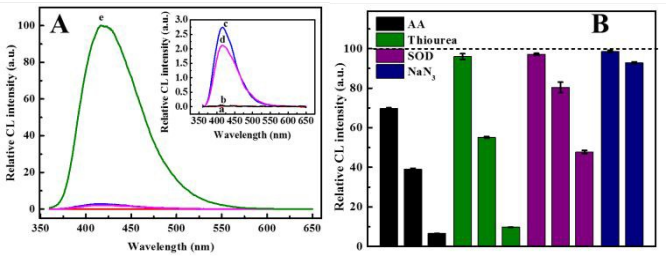

Fig. 4. (A) CL spectra for the luminol–H_2O_2–FeCo@NC-600 system. Reaction conditions: 1.0 mM luminol in 0.1 M Na_2CO_3–$NaHCO_3$ buffer (pH 11.3); 1.0 mM H_2O_2; 10 mg L^{-1} FeCo@NC-600. a: luminol+buffer; b: luminol+buffer+FeCo@NC-600; c: luminol+H_2O_2; d: luminol+H_2O_2+Fe^{III}-Co PBA; e: luminol+H_2O_2+FeCo@NC-600. (B) Effects of different radical scavengers on the CL emission of luminol–H_2O_2–FeCo@NC-600 system. Reaction conditions: 2 μM H_2O_2, 10 mg L^{-1} FeCo@NC-600, 10 μM luminol in 0.1 M Na_2CO_3-$NaHCO_3$ buffer (pH 11.3).

View Article Online
DOI: 10.1039/C9TB00797K

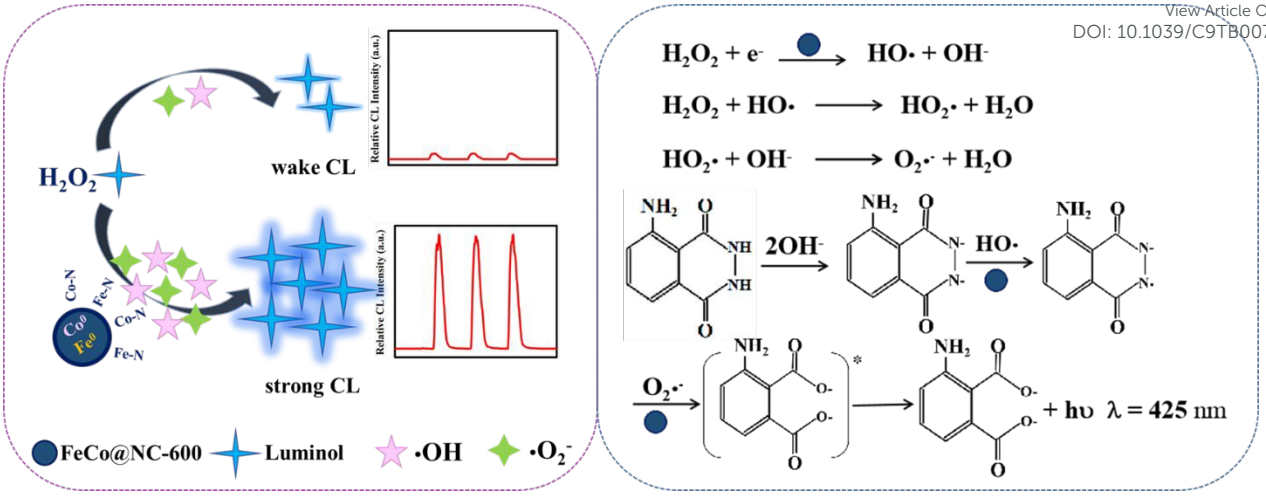

Fig. 5. Possible mechanism for the FeCo@NC catalyzed luminol-H_2O_2 CL system.

saturated experiment (Fig. S12, ESI†) proved that O_2 also plays an important role. Based on the above experimental results, the possibly catalytic CL mechanism by FeCo@NC-600 was shown in Fig. 5. In the luminol–H_2O_2–FeCo@NC-600 system, the enhancement of the CL intensity can be attributed to the formation of more superoxide anion radical ($•O_2^-$) and hydroxyl radical (•OH) that reacted with luminol anion radical via electron-transfer processes to produce the 3-APA* with a maximal emission peak at 425 nm. In the catalytic process, FeCo@NC-600 with excellent peroxidase-like catalytic activity accelerated the electron transfer and radical generation in the CL reaction because the FeCo alloy, metal-N bands and N-doped carbon are catalytic activity sites that catalyze the decomposition of H_2O_2 to generate more $•O_2^-$ and •OH.

3.3. Performance of FeCo@NC-based nanozyme CL biosensor for glucose

Based on peroxidase-like activity of FeCo@NC-600 and fast reaction of CL, we developed a glucose CL biosensor with high sensitivity, good selectivity, and stability. To realize glucose detection, first, the peroxidase-like activity of FeCo@NC-600 was optimized based on its catalytic role in the luminol–H_2O_2 reaction. Similar to other mimic enzymes, the peroxidase-like activity of FeCo@NC-600 was also dependent on its concentration, solution pH and substrate concentration. As shown in Fig. S13A to C (ESI†), the optimal activity of FeCo@NC-600 was observed at following conditions: 10 mg L^{-1} of FeCo@NC-600, pH 11.3 and 10 μM of luminol concentration. In the following studies, we selected above conditions as standard reaction conditions. Under the optimum conditions given above, the calibration curve was found to be linear from 1.0×10^{-8} to 4.0×10^{-5} mol L^{-1} for H_2O_2, and the regression equation is $\Delta I = 1343.5\ C_{H_2O_2}$ ($\times10^{-6}$ mol L^{-1}) − 799, $R^2 = 0.9984$ (n=15), where $C_{H_2O_2}$ is the concentration of H_2O_2 (Fig. S13D, ESI†). The limit of detection (LOD) for H_2O_2 is 2.5×10^{-9} mol L^{-1} (with an S/N ratio of 3). The relative standard deviation (RSD) was 1.84 % for 1.0×10^{-7} mol L^{-1} H_2O_2 (n = 11). The selectivity experiment was studied by examining the effect of coexistence interferences, including ions (Na^+, Ca^{2+}, K^+, Mg^{2+}, Al^{3+}, Zn^{2+}, Pb^{2+}, Ba^{2+}, Cr^{3+}, Ni^{2+}, NH_4^+, Cl^-, Br^-, NO_3^-, NO_2^-, SO_4^{2-}, SO_3^{2-}, HPO_4^{2-}, $H_2PO_4^-$ and PO_4^{3-}) and some biological molecules (leucine, glycine, alanie, L-phenylalanine and glutanmic acid, proline, methionine, serine, arginine and glutamine, tryptophane, cysteine, glutanthione and homocysteine, uric acid and ascorbic acid, HAS and IgG), on CL responses of 1.0×10^{-6} mol L^{-1} H_2O_2. Clearly, no obvious variance in CL signal (less than 5 %) was observed in the presence of these foreign substances (Table S4 and Fig. S14, ESI†).

Since glucose can be oxidized by dissolved oxygen with the help of GOx to produce gluconic acid and H_2O_2, we then applied FeCo@NC-600 for sensitive CL detection of glucose. As shown in Fig. 6A, the CL responses increased linearly with glucose concentrations in the 1.0×10^{-8} to 1.0×10^{-5} mol L^{-1} range. The regression equation can be described as follows: $\Delta I = 1366.0\ C_{glucose}$ (μmol L^{-1}) − 241, $R^2 = 0.9954$ (n=11). The detection limit for glucose is 8.5×10^{-9} mol L^{-1} at the signal-to-noise (S/N) ratio of 3. The relative standard deviation (RSD) is 1.65 % for 0.1 μmol L^{-1} glucose. We compared the linear detection range and LOD with other CL methods for glucose in previous works. As shown in Table S4, the proposed method shows high sensitivity with low LOD. To demonstrate the practical application of the proposed method for glucose detection in real samples, first, the effects of glucose analogues (including fructose, lactose, sucrose, maltose and starch) on CL response of the

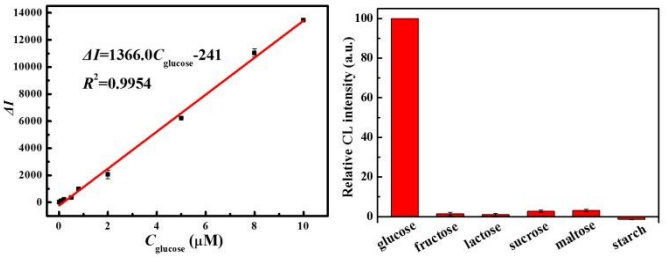

Fig. 6. (A) The linear relationship between net CL intensity and concentration of glucose. Experiment conditions: 10 μM luminol in 0.1 M Na_2CO_3-$NaHCO_3$ buffer solution (pH 11.3), 10 mg/L FeCo@NC-600. (B) Selectivity assay for the detection of glucose by monitoring the relative CL intensity. The concentration of glucose, fructose, lactose, sucrose, maltose and starch were 0.5, 5, 10, 0.5, 0.5, and 5 μM, respectively. Error bars were acquired from three replicates determination.

Journal Name ARTICLE

DOI: 10.1039/C9TB00797K

luminol–H_2O_2–FeCo@NC-600 system were examined to evaluate the selectivity. Fig. 6B indicates that no obvious CL is produced, suggesting good selectivity of the proposed method for glucose. Then, the FeCo@NC-600 composites were applied in the luminol–H_2O_2 system to determine glucose level in human serum samples. From Table 1, the result of glucose detection in serum samples agreed well with the values obtained from the GOx-PAP-based clinical method. Therefore, the FeCo@NC-600 as a new peroxidase mimetic exhibits great potential for monitoring glucose level in clinical diagnosis.

Table 1. Results of glucose determination in human serum samples by the proposed method and the GOx-PAP method

Sample	Proposed method (mM, *n*=3)*	GOx-PAP method (mM)	RSD (%)
Serum 1	4.12 ± 0.24	3.90	2.34
Serum 2	5.05 ± 0.23	5.10	1.66
Serum 3	7.95 ± 0.20	7.80	1.28

* mean ± standard deviation (*n*=3)

3.4. Stability of the FeCo@NC-600 peroxidase mimetic

Another advantage of the FeCo@NC-600 peroxidase mimetic is its enhanced stability. To support this, as a comparison, we synthesized FeCo NPs through direct reduction method.[4] Bad crystalline state was shown in XRD spectra of the FeCo NPs (Fig. S15, ESI†). Then, the stability of FeCo NPs and FeCo@NC-600 was evaluated under the same experimental conditions. As shown in Fig. S16 (ESI†), during 25-day storage of the FeCo NPs and FeCo@NC-600 aqueous solutions with same concentration at room temperature, no significant decrease in the peroxidase mimetic activity of FeCo@NC-600 toward luminol oxidation by H_2O_2 is observed, while FeCo NPs display a significant loss of activities (below 30 % at 25 days). This is probably because the exposed FeCo alloy NPs surface is easy oxidized, while the graphite carbon layer on the FeCo@NC-600 surface plays a protective role and greatly improved the stability[24,43] of FeCo@NC-600.

3. Conclusion

In summary, FeCo alloy@nitrogen-doped carbon composite was successfully fabricated by a facile one step carbonization of the Fe^{III}-Co Prussian blue analogues. The optimized FeCo@NC-600 has highly peroxidase-like activity that catalyzes oxidation of TMB, ABTS and OPD by H_2O_2 to generate color products, and luminol oxidation by H_2O_2 to generate strong CL emission with more than 85-fold enhancement effect. On this basis, a new FeCo@NC hybrid-based nanozyme CL biosensor for glucose was developed, which exhibited an outstanding performance for glucose sensing, including wide linear range of 10 nM – 10 μM, low detection limit of 8.5 nM, fast response, long-term storage stability. The potential application of the proposed method was successfully demonstrated by its use in detecting glucose level in human serum samples with high precision and good reproducibility. The simple strategy for the construction of the FeCo@NC promises great potential for the development of highly active nanozyme for applications in biochemical detection and medical diagnostics.

Conflicts of interest

There are no conflicts to declare.

Acknowledgements

Financial support from the National Natural Science Foundation of China (No. 51678485) is gratefully acknowledged.

References

1 P. Statements, *Diabetes Care*, 1991, **55**, 625–629.
2 D.M. Nathan, *N. Engl. J. Med.*, 1993, **328**, 1676–1685.
3 X. Cao, N. Wang, S. Jia and Y.H. Shao, *Anal. Chem.*, 2013, **85**, 5040–5046.
4 Y.J. Chen, H.Y. Cao, W.B. Shi, H. Liu and Y.M. Huang, *Chem. Commun.*, 2013, **49**, 5013–5015.
5 F. Lou, Z.S. Lu, F. X. Hu and C.M. Li, *J. Electroanal. Chem.*, 2017, **787**, 125–131.
6 W.S. Zou, C.H. Ye, Y.Q. Wang, W.H. Li and X.H. Huang, *Sens. Actuators B*, 2018, **271**, 54–63.
7 X.X. Mao, Y.W Lu, X.D. Zhang and Y.M. Huang, *Talanta*, 2018, **188**, 161–167.
8 X.L. Yi, W.F. Dong, X.D Zhang, J.X Xie and Y.M Huang, *Anal. Bioanal. Chem.*, 2016, **408**, 8805–8812.
9 H. Chen, Q. Gao, J.Z. Li and J.M. Lin, *J. Photochem. Photobiol. C*, 2016, **27**, 54–71.
10 A. M. Garcia-Campana, W. R. G. Baeyens, Chemiluminescence in analytical chemistry, Marcel Dekker, N. York, 2001.
11 A. Khataee, M. Iranifam, M. Fathinia and M. Nikravesh, *Spectrochim. Acta A*, 2015, **134**, 210–217.
12 Z.F. Zhang, H. Cui, C.Z. Lai and L.J. Liu, *Anal. Chem.*, 2005, **77**, 3324–3329.
13 P. Yang, S.Y. Jin, Q.Z. Xu, and S.H. Yu, *Small*, 2013, **9**, 199–204.
14 H.L. Yu and Y. He, *Sens. Actuators B*, 2015, **209**, 877–882.
15 A.K. Singh and Q. Xu, *ChemCatChem*, 2013, **5**, 652–676.
16 R.S. Ruoff, D.C. Lorents, B. Chan, R. Malhotra and S. Subramoney, *Science*, 1993, **259**, 346–348.
17 L.M. Cao, Z.P. Lin, J.L. Huang, X. Yu, X.X. Wu, B.D. Zhang, Y.F. Zhan, F.Y. Xie, W.H. Zhang, J. Chen, W.G. Xie, W.J. Mai and H. Meng, *Int. J. Hydrogen Energ.*, 2017, **42**, 876–885.
18 Cicero W.B. Bezerra, L. Zhang, K.C. Lee, H.S. Liu, Aldaléa L.B. Marques, Edmar P. Marques, H.J. Wang and J.J. Zhang, *Electrochim. Acta*, 2008, **53**, 4937–4951.
19 X.N. Li, J.Y.Liu, A. I. Rykov, H.X. Han, C.Z. Jin, X. Liu and J.H. Wang, *Appl. Catal. B-Environ.*, 2015, **179**, 196–205
20 (a) S. Margadonna, K. Prassides and A.N. Fitch, J. Am. Chem. Soc., 2004, **126**, 15390–15391; (b) A. Derobertis, A. Bellomo and D. Demarco, *Talanta*, 1976, **23**, 732–734.
21 R. Qiang, Y.C. Du, H.T. Zhao, Y. Wang, C.H. Tian, Z.G. Li, X.J. Han and P. Xu, *J. Mater. Chem. A*, 2015, **3**, 13426–13434.
22 D.R. Li, X.H. Liang, W. Liu, J.N. Ma, Y.A. Zhang, G.B. Ji and W. Meng, *J. Colloid. Interf. Sci.*, 2017, **507**, 131–138.
23 B.Y. Guan, Y. Lu, Y. Wang, M.H. Wu and X.W. Lou, *Adv. Funct. Mater.*, 2018, **28**, 1706738.
24 P.W. Cai, S.Q. Ci, E.H. Zhang, P. Shao, C.S. Cao, Z.H. Wen, *Electrochim. Acta*, 2016, **220**, 354–362.
25 J.B. Ayers and W.H. Waggoner, *J. Inorg. Nucl. Chem.*, 1971, **33**, 721–733.

26 K. Itaya, I. Uchida and V.D. Neff, *Acc. Chem. Res.*, 1986, **19**, 162–168.
27 G. Zhao, J.J. Feng, Q.L. Zhang, S.P. Li and H.Y. Chen, *Chem. Mater.*, 2005, **17**, 3154–3159.
28 Y. Hou, Z.H. Wen, S.M. Cui, S.Q. Ci, S. Mao and J.H. Chen, *Adv. Funct. Mater.*, 2015, **25**, 872–882.
29 Q.X. Lai, L.R. Zheng, Y.Y. Liang, J.P. He, J.X. Zhao and J.H. Chen, *ACS Catal.*, 2017, **7**, 1655–1663.
30 Y. Yang, Z. Lin, S. Gao, J. Su, Z. Lun, G. Xia, J. Chen, R. Zhang and Q. Chen, *ACS Catal.*, 2017, **7**, 469–479.
31 X.W. Teng, D. Black, N.J. Watkins, Y.L. Gao and H. Yang, *Nano Lett.*, 2003, **2**, 261–264.
32 H. Zhu, J. Zhang, R. Yanzhang, M. Du, Q. Wang, G. Gao, J. Wu, G. Wu, M. Zhang and B. Liu, *Adv. Mater.*, 2015, **27**, 4752–4759.
33 M.C. Biesinger, B.P. Payne, A.P. Grosvenor, L.W. Lau, A.R. Gerson and R.S.C. Smar, *Appl. Surf. Sci.*, 2011, **257**, 2717–2730.
34 M. Li, T.T. Liu, X.J. Bo, M. Zhou and L.P. Guo, *J. Mater. Chem. A*, 2017, **5**, 5413–5425.
35 G.L. Lu, Y.L. Zhu, L. Lu, K.L. Xu, H.M. Wang, Y.H. Jin, Z.Y. Jason Ren, Z.N. Liu and W. Zhang, *J. Power Sources*, 2016, **315**, 302–307.
36 Q.L. Huang, S.L. Wang, Y. Zhang, B.W. Yu, L.Z. Hou, G. Su, S.S. Ma, J. Zou and H. Huang, *J. Phys. Chem. C*, 2016, **120**, 3139–3144.
37 J.B. Xi, Y.T. Xia, Y.Y. Xu, J.W. Xiao and S.A. Wang, *Chem. Commun.*, 2015, **51**, 10479–10482.
38 C. Zhao, C. Xiong, X.K. Liu, M. Qiao, Z.J. Li, T.W. Yuan, J. Wang, Y.T. Qu, X.Q. Wang, F.Y. Zhou, Q. Xu, S.Q. Wang, M. Chen, W.Y. Wang, Y.F. Li, T. Yao, Y.E. Wu and Y.D. Li, *Chem. Commun.*, 2019, **55**, 2285–2288.
39 B.L. Xu, H. Wang, W.W. Wang, L.Z. Gao, S.S. Li, X.T. Pan, H.Y. Wang, H.L. Yang, X.Q. Meng, Q.W. Wu, L.R. Zheng, S.M. Chen, X.H. Shi, K.L. Fan, X.Y. Yan and H.Y. Liu, *Angew. Chem. Int. Ed.*, 2019, **58**, 4911–4916.
40 W.J. Ma, J.J. Mao, X.T. Yang, C. Pan, W.X. Chen, M. Wang, P. Yu, L.Q. Mao and Y.D. Li, *Chem. Commun.*, 2019, **55**, 159–162.
41 Y.H. Hu, X.J.J. Gao, Y.Y. Zhu, F. Muhammad, S.H. Tan, W. Cao, S.C. Lin, Z. Jin, X.F. Gao and H. Wei, *Chem. Mater.*, 2018, **30**, 6431–6439.
42 J.B. Xi, Y.T. Xia, Y.Y, Xu, J.W. Xiao and S. Wang, *Chem. Commun.*, 2015, **51**, 10479–10482.
43 P.W. Cai, Y. Hong, S.Q, Ci and Z.H. Wen, *Nanoscale*, 2016, **8**, 20048–20055.
44 M. Gopiraman, S. G. Babu, Z. Khatri, W. Kai, Y. A. Kim, M. Endo, R. Karvembu and I. S. Kim, *Carbon*, 2013, **62**, 135–148.
45 X.T. Pan, L.X, Bai, H, Wang, Q.Y. Wu, H.Y. Wang, S. Liu, B.L. Xu, X.H. Shi and H.Y. Liu, *Adv. Mater.*, 2018, **30**, 1800180.
46 C. H. Christensen, K. Johannsen, E. Törnqvist, I. Schmidt, H. Topsøe and C. H. Christensen, *Catal. Today*, 2007, **128**, 117–122.
47 P.W. Cai, J.H. Huang, J.X. Chen, and Z.H. Wen, *Angew. Chem. Int. Ed.* 2017, **56**, 4858–4861.
48 Zexing Wu, Ping Li, Qing Qin, Zijian Li, Xien Liu, *Carbon*, 2018, **139**, 35–44.
49 M.J. Chaichi and M. Ehsani, *Sens. Actuators B*, 2016, **223**, 713–722.
50 J.X. Xie, W.J. Chen, X.X. Wu, Y.Y. Wu and H. Lin, *Anal. Methods*, 2017, **9**, 974-979.
51 T. Hallaj, M. Amjadi, Z.L. Song and R. Bagheri, *Microchim. Acta*, 2018, **185**, 67.
52 K. Zargoosh, M.J. Chaichi, M. Shamsipur, S. Hossienkhani, S. Asghari and M. Qandalee, *Talanta*, 2012, **93**, 37– 43.
53 Y.F. Fan and Y.M. Huang, *Analyst*, 2012, **137**, 1225–1231.
54 W.B. Shi, X.D. Zhang, S.H. He and Y.M. Huang, *Chem. Commun.*, 2011, **47**, 10785–10787.
55 A. Khataee, M. H. Irani-nezhad, J. Hassanzadeh, *Microchim. Acta*, 2018, **185**, 190.
56 F.Q. Luo, Y.L. Lin, L.Y. Zheng, X.M. Lin and Y.W. Chi, *ACS Appl. Mater. Interfaces*, 2015, **7**, 11322−11329.

View Article Online
DOI: 10.1039/C9TB00797K

View Article Online
DOI: 10.1039/C9TB00797K

Table of Content Entry

Directly pyrolyzing Prussian blue analogue produces the FeCo@NC with high and stable peroxidase-like activity that catalyzes luminol oxidation by H_2O_2 to generate strong CL emission with more than 85-fold enhancement, and this finding results in a new CL biosensor for glucose.